Journal of Analytical and Applied Pyrolysis 196 (2026) 107787

Contents lists available at ScienceDirect

Journal of Analytical and Applied Pyrolysis

journal homepage: www.elsevier.com/locate/jaap

Deep learning prediction of cathode thermal degradation kinetics for battery safety

Yuxin Zhou [a], Yichao Zhang [a], Peiyi Sun [a], Yifei Ding [a], Shaorun Lin [a], Xinyan Huang [a,b,*]

[a] Department of Building Environment and Energy Engineering, The Hong Kong Polytechnic University, Hong Kong
[b] Research Institute for Smart Energy, The Hong Kong Polytechnic University, Hong Kong

ARTICLE INFO

Keywords:
Li-ion battery
Cathode materials
Thermal decomposition kinetics
Reductive attack
Convolutional neural network
Kinetic compensation effect

ABSTRACT

Thermal decomposition of lithium-ion battery cathode materials poses a critical safety challenge for the design and management of high-energy batteries. Accurate determination of reaction kinetic parameters is essential for understanding subsequent thermal runaway behavior. A deep learning framework was developed to automatically predict kinetic parameters from multi-rate differential thermogravimetry (DTG) curves of pristine (non-delithiated) nickel–cobalt–manganese oxide (NCM) cathode materials under reductive gas attack. By jointly fitting the Johnson Mehl Avrami (JMA) model to experimental benchmarks, we established material-specific kinetic compensation effect (KCE) manifolds for four commercial NCM cathode materials (NCM811, 622, 523, and 111). These manifolds guided the construction of a synthetic dataset containing 20,000 multi-rate samples, designed to emulate complex peak-shift dynamics and instrumental noise. A specialized one-dimensional convolutional neural network (1D CNN) was engineered to process synchronized three-rate DTG sequences (10, 30, and 60 K·min^{-1}), allowing the model to implicitly learn the governing kinetic laws from raw signal topology. On the synthetic training set, the multi-rate CNN achieved an exceptional R^2 of 0.94 for both activation energy (E_a) and pre-exponential factor (lg$A$), with validation set R^2 of 0.92. Beyond numerical precision, the CNN faithfully reconstructed composition-specific KCE lines with slope deviations under 0.5%, proving its ability to capture subtle "kinetic fingerprints" without manual feature engineering. While delithiated cathodes exhibit more complex behaviors, this pristine-based foundation provides a scalable and reproducible trajectory for high-throughput screening and future transfer learning to diverse battery states of charge. By reducing diagnostic latency from hours to milliseconds, this "kinetics intelligence" approach provides a scalable and reproducible tool for high-throughput cathode screening and real-time safety assessment in industrial-scale battery management.

1. Introduction

The global energy landscape is rapidly transitioning towards low-carbon solutions, establishing lithium-ion batteries (LIBs) as the cornerstone technology for electric vehicles (EVs), grid-scale energy storage systems, and portable electronics. This growth is marked by a dramatic surge in demand; for instance, the annual demand for EVs has grown at 31% until 2020, with forecasts indicating that EV production could exceed 55 million units by 2037 [1]. To meet the increasing mileage requirements of EVs, the pursuit of LIBs with higher energy densities remains relentless [2]. However, the pursuit of higher energy density inherently introduces increased safety concerns. Materials with elevated energy density often exhibit lower thermal stability [3], potentially leading to catastrophic safety failures known as thermal runaway (TR) [4]. TR is a complex chain of exothermic reactions, including cathode decomposition, electrolyte degradation, and the rupture of the solid-electrolyte interphase (SEI) film [5]. Gaining a thorough understanding and effective suppression of these exothermic processes is fundamental to ensuring battery safety.

Cathode materials are critical determinants of both the performance and safety of LIBs [3]. For example, the energy density is directly linked to the specific capacity and operating voltage of the cathode [3]. High-nickel ternary layered oxides ($LiNi_xMn_yCo_zO_2$) are the material of choice due to their superior capacity. Nevertheless, high nickel content significantly compromises thermal stability [3]. Upon charging to high potential, the cathode undergoes delithiation, increasing the valence of the transition-metal ions and facilitating undesired reactivity with the

* Corresponding author at: Department of Building Environment and Energy Engineering, The Hong Kong Polytechnic University, Hong Kong.
E-mail address: xy.huang@polyu.edu.hk (X. Huang).

https://doi.org/10.1016/j.jaap.2026.107787
Received 15 November 2025; Received in revised form 30 March 2026; Accepted 3 April 2026
Available online 8 April 2026

Nomenclature

Symbol	DescriptionUnit
A	Pre-exponential factors^{-1}
E_a	Activation energykJ·mol^{-1}
$f(\alpha)$	Reaction model function-
$k(T)$	Rate constants^{-1}
n	Reaction order-
R	Universal gas constantJ·mol^{-1}
R^2	Coefficient of determination-
T	TemperatureK
T_p	Peak temperatureK
t	Times
α	Conversion fraction-
β	Heating rateK·min^{-1}
σ	Standard deviation of noise-

electrolyte [6]. Critically, the inherent structural instability leads to oxygen release, which reacts violently and exothermically with the electrolyte and the lithiated graphite anode, accelerating the heat generation and potentially triggering TR [6]. Therefore, accurate assessment and enhancement of the thermal safety performance of cathode materials are of paramount importance.

The thermal decomposition of delithiated NCM cathodes is a complex physiochemical process involving sequential reactions and oxygen release. Wang et al. [7] established the fundamental correlations between material composition and kinetic parameters across multi-stage decomposition pathways. Furthermore, studies indicate that under internal fault or abuse conditions, reducing gases (H_2, CO, C_2H_2 etc.) are generated from the negative electrode. The presence of these reductive gases drastically accelerates the decomposition of the cathode material, inducing accelerated structural phase transitions, enhanced oxygen release, and intense heat generation. The reductive attack can initiate at temperatures below 80℃ and disrupt the chemical interactions across the cell components, propelling the thermal failure [8].

Building upon this discovery, our previous work conducted an in-depth study on the thermal degradation behavior of cathode materials under reductive gas attack (Fig. 1). We established a TGA experimental system to obtain thermal performance data of cathode materials under the combined effect of high temperature and a reductive atmosphere. Utilizing these data, we developed an Artificial Neural Network (ANN) model. This model takes macro-parameters, such as elemental composition, gas concentration, and heating rate—as input to predict the material's apparent thermal performance, and employed the analytic hierarchy process (AHP) to provide a preliminary safety rating. This earlier research not only deepened the understanding of cathode stability but also offered valuable insights for predicting the macroscopic thermal stability of novel cathode materials [9].

Previous studies have demonstrated that artificial neural network (ANN) models can efficiently predict the macroscopic thermal properties of materials. However, such models are essentially empirical or phenomenological in nature and lack the ability to quantitatively describe and physically interpret the microscopic kinetic mechanisms governing material decomposition. Therefore, to extract more physically meaningful quantities from thermal analysis data and enable a deeper evaluation of thermal stability, chemical reaction kinetics analysis provides an effective approach. By characterizing key kinetic parameters such as the energy barrier (activation energy, Ea) that reactant molecules must overcome, the collision frequency (pre-exponential factor, lgA), and the entropy change during reaction, the intrinsic mechanisms of thermal decomposition can be quantitatively revealed. Chemical reaction kinetics models based on the Arrhenius equation have become a fundamental tool for thermal safety assessment.

In most studies, thermal behaviors are measured by adiabatic reaction calorimetry (ARC) or differential scanning calorimetry (DSC), and the kinetic parameters—including pre-exponential factor, activation energy, mechanism function, and reaction enthalpy—are subsequently determined to elucidate reaction mechanisms and predict the thermal stability of cell components [10–13]. For example, DSC data combined with the Kissinger and Ozawa methods have been widely used to investigate the decomposition kinetics of various cathode materials, such as Li_xCoO_2 *and* $Li_x(Ni_{0.33}Mn_{0.33}Co_{0.33})O_2$, yielding corresponding activation energies and reaction orders [11,14]. Gao et al. further employed thermogravimetric–differential thermal analysis (TG–DTA) and applied the Flynn–Wall–Ozawa (FWO) and Kissinger methods to determine the activation energy, reaction order, and kinetic equation of the lithium-rich manganese-based cathode $Li_{1.16}(Ni_{0.25}Mn_{0.0.75})_{0.84}O_2$. Based on these results, an optimized two-step sintering process was developed, leading to a highly crystalline material with excellent electrochemical performance.

Despite its widespread use in diverse fields, the Kissinger method still suffers from intrinsic theoretical limitations. It relies solely on the peak temperature of DSC curves for kinetic analysis and assumes a single-step

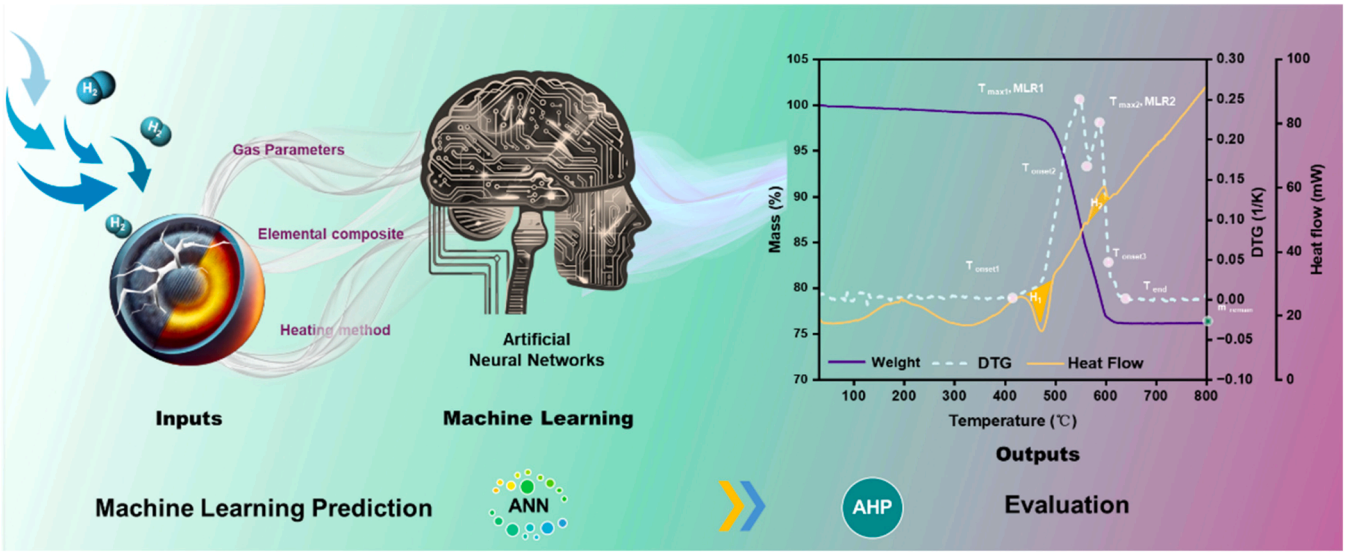

Fig. 1. A method to predict and assess the stability and safety of LIB cathode materials.

reaction with a strictly exponential temperature dependence [15–17]. These oversimplified assumptions are often invalid in complex multi-step reaction systems, leading to kinetic models that deviate from the actual decomposition pathways. To overcome these limitations, advanced data-driven frameworks, such as the Chemical Reaction Neural Network (CRNN) and its Bayesian extensions, have been recently proposed. These approaches can account for sequential multi-step reactions and non-exponential temperature dependence, while also enabling the quantification of thermal-kinetic uncertainties. Models developed under this framework have shown improved accuracy and stronger physical consistency in describing the thermal decomposition of nickel–cobalt–manganese (NCM) oxide cathodes. Consequently, this paradigm opens new possibilities for leveraging artificial intelligence to learn and interpret the thermokinetic characteristics of materials, bridging the gap between empirical prediction and mechanism-oriented kinetic modeling [18,19].

Machine learning approaches have gained attention in thermal analysis, with convolutional neural networks (CNNs) showing promise for processing TGA data [20–23]. CNNs can analyze complete time-series while preserving sequential relationships, making them suitable for differential thermogravimetric (DTG) curve analysis [24,25]. The hierarchical structure allows early layers to detect basic curve features while deeper layers identify complex thermal patterns [26]. This capability addresses limitations in current practice. Traditional kinetic analysis typically extracts only peak temperatures, onset points, and mass loss values from DTG curves, potentially missing mechanistic information encoded in the complete profile [27,28]. Battery cathode materials present particular challenges since thermal decomposition often involves overlapping reaction steps that are difficult to separate using conventional methods [6,29,30].

Building on these developments in CNN applications for thermal analysis, one-dimensional CNNs may offer advantages by treating thermal analysis as a sequential process rather than independent measurements. The parameter-sharing mechanism allows patterns learned in one temperature region to be applied elsewhere, which could improve performance across different experimental conditions [31–33]. However, the effectiveness for kinetic parameter prediction requires validation with diverse datasets, and model interpretability within established kinetic frameworks remains an open question. Although thermal analysis techniques are widely used for battery material safety assessment, current methods for extracting reaction kinetic parameters still rely primarily on multi-heating rate experiments and manual model fitting [34,35]. While machine learning has been applied to thermal property prediction, existing approaches remain phenomenological and lack direct correlation between DTG features and physically meaningful kinetic parameters [36].

This study presents a deep learning framework that directly predicts activation energy (Ea) and pre-exponential factor (A) from DTG data. We constructed a physically consistent synthetic multi-heating-rate DTG dataset based on classical kinetic models and Kissinger-derived parameters, providing a foundation for large-scale supervised learning under realistic thermal decomposition conditions. A specialized one-dimensional convolutional neural network was designed to extract DTG curve patterns and integrate material-specific descriptors, achieving accurate kinetic parameter prediction across multiple NCM materials. This framework enables rapid kinetic parameter estimation from multi-heating-rate DTG inputs experiments, providing an efficient tool for cathode material safety assessment. By directly extracting mechanistic information from thermal data, this work bridges empirical analysis and fundamental decomposition understanding, providing strong support for safer material development and more reliable battery materials design.

2. Experiments and methodologies

2.1. Materials and TGA analysis

Commercial NCM cathode materials with varying elemental compositions (NCM811, NCM622, NCM523, NCM111) were obtained from Cardo and used pristine (non-delithiated) state without further purification. Prior to testing, all samples and crucibles were dried at 80℃ for 12 h to eliminate moisture effects. This study specifically utilizes pristine materials to establish a high-fidelity kinetic baseline, ensuring that the developed 1D CNN internalizes fundamental reaction topologies without the interference of stochastic noise associated with delithiation, such as residual electrolyte artifacts or state-of-charge (SOC) gradients.

TGA analysis was performed on a PerkinElmer STA6000 simultaneous thermal analyzer under reducing gas atmospheres. A mixture of hydrogen and argon at 5% H_2 was used to simulate internal fault conditions in lithium-ion batteries. Approximately 5–7 mg of each material was subjected to non-isothermal heating from room temperature to 800℃ at heating rates of 10, 30, and 60 K/min. Gas flow rates were maintained at 100 mL/min to investigate the effect of gas dynamics on thermal decomposition behavior. Each experimental condition was replicated at least twice, with relative errors maintained within ±2%.

2.2. Kinetic parameter estimation and synthetic DTG dataset generation

The Kissinger method [37,38] is derived from the fundamental Arrhenius rate equation for thermally activated processes. For a solid-state reaction following first-order kinetics, the rate of conversion can be expressed as:

$$\frac{d\alpha}{dt} = A\exp(-\frac{E_a}{RT})f(\alpha) \tag{1}$$

where α is the degree of conversion, t is time, A is the pre-exponential factor (s^{-1}), E_a is the activation energy (kJ/mol), R is the universal gas constant (8.314 J/(mol·K)), T is the absolute temperature (K), and $f(\alpha)$ is the reaction model function. In all Arrhenius and Kissinger computations, E_a was converted to kJ/mol to remain consistent with R= 8.314 J/(mol·K).

At the maximum decomposition rate (DTG peak temperature T_p), the Kissinger equation relates heating rate to peak temperature: Under non-isothermal conditions with a constant heating rate $\beta = dT/dt$, the rate equation becomes:

$$\ln(\frac{\beta}{T_p^2}) = \ln(\frac{AR}{E_a}) - \frac{E_a}{RT_p} \tag{2}$$

Applying this condition and assuming $f(\alpha) = (1-\alpha)^n$ where n is the reaction order, Kissinger derived the following relationship:

$$\ln(\frac{\beta}{T_p^2}) = -\frac{E_a}{R}\cdot\frac{1}{T_p} + \ln(\frac{AR}{E_a}) \tag{3}$$

where T_p is the peak temperature corresponding to the maximum decomposition rate at heating rate β. For experiments at multiple heating rates, plotting $\ln\left(\frac{\beta}{T_p^2}\right)$ versus $1/T_p$ yields a straight line with:

$$m = -\frac{E_a}{R} \tag{4}$$

The logarithmic pre-exponential factor is calculated as:

$$\lg A = \log_{10}(A) = \frac{1}{\ln(10)}[b + \ln(\frac{E_a}{R})] \tag{5}$$

For the first approximation, we choose the peak temperature for the reaction of each cathode materials and plot $1/T_p$ against $\ln\left(\frac{\beta}{T_p^2}\right)$ under

different heating rates. The TG data of 10, 30, and 60 K/min are used to determine kinetic parameters, as plotted in Fig. 2. The activation energy can be estimated from the slope of $-\frac{E_a}{R}$ by a linear fit of three experimental points, and substituting back into Eq. 5 gives the pre-exponential factor. Table 1 lists the obtained T_p, lg A and E_a as well as fitting condition (R^2) for the proposed kinetics under three heating rates.

It should be noted that the kinetic parameters derived from the preliminary Kissinger analysis Table 1 served strictly as a first-order approximation to guide the construction of the synthetic dataset. E_a values are reported in kJ/mol, A is the pre-exponential factor in s^{-1}, R^2 refers to the linear fit of the Kissinger plot. These values were used to define the boundaries of the realistic experimental parameter space, ensuring the training manifold aligns with the physical behavior of NCM cathodes. With the kinetic parameters obtained from Kissinger analysis, we proceeded to generate synthetic DTG curves using the Johnson–Mehl–Avrami (JMA) kinetic model [38,39]. This model is widely used for solid-state decomposition because it captures the nucleation and growth features that govern many thermally driven reactions in battery materials. The corresponding rate expression is:

$$\frac{d\alpha}{dt} = A\exp(-\frac{E_a}{RT})\cdot n(1-\alpha)[-\ln(1-\alpha)]^{\frac{n-1}{n}} \quad (6)$$

The term $n(1-\alpha)[-\ln(1-\alpha)]^{\frac{n-1}{n}}$ is the JMA reaction model function, which captures the complexity of the decomposition mechanism [40,41].

Importantly, this JMA-KCE synthetic dataset was designed as a physics-constrained manifold rather than a mere simplification. By systematically varying the parameters within realistic bounds derived from our 12 initial experimental sets, we ensure the 1D CNN encounters a comprehensive spectrum of peak topologies—including varying widths, symmetries, and temperature shifts. This approach forces the model to learn the fundamental mapping between thermogravimetric gradients and reaction kinetics, effectively acting as a noise-robust feature extractor capable of generalizing to real experimental signals.

Synthetic DTG sequences were numerically derived by solving the JMA kinetic equation across three heating rates (10, 30, and 60 K·min^{-1}) over a temperature window of 30–800 °C. To ensure computational efficiency during neural network training, the resulting curves were interpolated and resampled to 200 equidistant temperature points, with the signal defined as the conversion rate $d\alpha/dT$. To maintain physical rigor, the sampling of E_a and lg A was predominantly linked via the material-specific KCE relationships established in our experimental benchmarks.

Table 1
Kinetic Parameters and Possible value via Kissinger's Method.

Cathode materials	β (K/min)	T_p (K)	E_a (kJ/mol)	lg A (s^{-1})	R^2
NCM811	10	547	71.02	1.864	0.9915
	30	617			
	60	684			
NCM622	10	587	89.52	2.849	0.9712
	30	644			
	60	707			
NCM523	10	613	111.56	4.016	0.9714
	30	683			
	60	712			
NCM111	10	606	93.92	2.976	0.9969
	30	671			
	60	726			

However, to prevent the model from over-fitting strictly to these linear manifolds, a subset of samples was deliberately drawn from a broader plane to introduce controlled variability. To bridge the gap between ideal simulations and real-world measurements, each synchronized three-rate sample was peak-normalized and superimposed with a composite noise profile, including baseline drift, signal-dependent fluctuations, and stochastic spike artifacts. The final dataset comprised 20000 multi-rate samples, evenly distributed among the four NCM cathodes (5000 each). Each record containing the synchronized DTG triplet, heating rate descriptors, and ground-truth kinetic labels was randomly partitioned into training, validation, and test sets to facilitate the end-to-end learning process.

2.3. Convolutional neural network architecture and training

To overcome the simplifications of the Kissinger approach, which is limited by its reliance on peak-temperature points, we developed a 1D CNN framework. This model utilizes the full DTG waveform rather than isolated points, significantly improving prediction stability against experimental noise and baseline fluctuations. A one-dimensional convolutional neural network (1D CNN) was developed for end-to-end prediction of kinetic parameters from mutli heating rate DTG curves. The 1D convolution operation applies learnable filters across the temperature dimension according to:

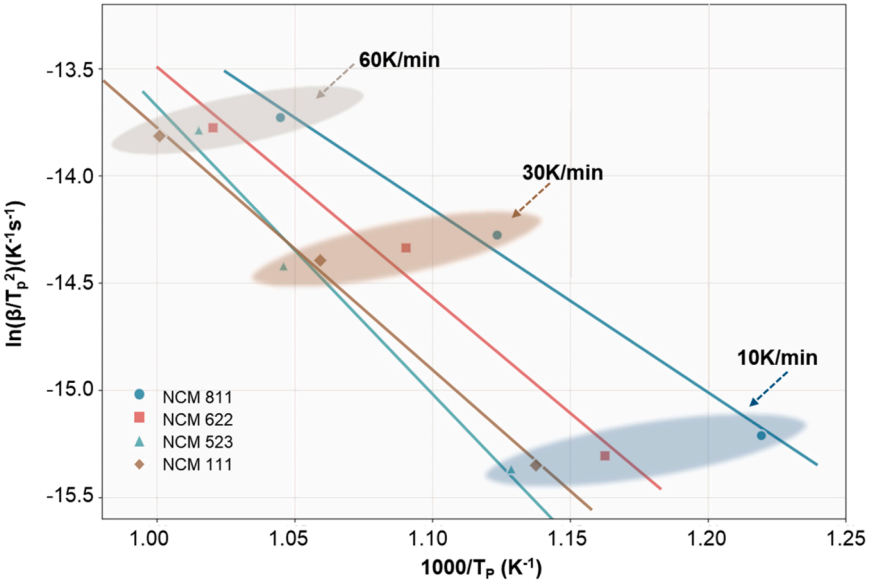

Fig. 2. Correlations of heating rates and peak temperatures.

$$Y_{c,t} = \sum_{i=0}^{k-1} W_{c,i} \cdot X_{t+i} + b_c \tag{7}$$

where $W_{c,i}$ represents the learnable weights of filter c, b_c is the bias term, and different kernel sizes enable multi-scale feature extraction from DTG sequences.

The architecture of the developed CNN model has been shown in Fig. 3 is designed to resolve kinetic descriptors directly from multi-scale thermal trajectories. The model processes a synchronized 3-channel input tensor consisting of DTG sequences resampled to 200 equidistant points. This multi-channel configuration is fed into a shared 1D-CNN backbone comprising four convolutional layers. To capture both the broad thermal envelopes and fine-grained mechanistic features, the filter channels expand from 32 to 256 while kernel sizes are systematically tapered from 15 to 3. Each convolutional stage integrates batch normalization, ReLU activation, and dropout (0.2–0.3) to ensure numerical stability and suppress overfitting during feature extraction.

$$\hat{y} = f_{CNN}(X_{DTG}) \oplus f_{FC}(X_{aux}) \rightarrow [E_a, \lg A] \tag{8}$$

where X_{DTG}represents the 200-point DTG sequence, X_{aux} denotes the 7-dimensional auxiliary features, and $\oplus$ indicates the concatenation operation.

To ensure numerical stability and balanced gradient descent, all input sequences and target kinetic parameters (E_a and lg A) were standardized using Z-score normalization prior to the training phase. The standardized value X_{norm} is defined as:

$$X_{norm} = (X - \mu)/\sigma \tag{9}$$

where X represents the raw input, while μ and σ denote the mean and standard deviation of the training dataset, respectively.

The dataset comprises 20,000 synthetic multi-rate samples, evenly distributed with 5000 instances generated for each stoichiometry including NCM811, 622, 523, and 111. These data were partitioned into training, validation, and test sets according to a 70/15/15 ratio. Stratification by material type was strictly maintained during partitioning to ensure that each subset provides a balanced and representative sampling of the kinetic manifolds across the NCM series. Training was conducted for 140 epochs using a batch size of 128 and the Mean Squared Error (MSE) loss function. Optimization utilized the Adam optimizer with an initial learning rate of 3×10^{-4} and a weight decay of 10^{-4}. To facilitate smooth convergence in the complex parameter space, a cosine-annealing learning-rate schedule with $T_{max} = 140$ was adopted, replacing the conventional step-wise decay.

The model was trained for up to 140 epochs with batch size 128 using MSE loss:

$$L_{MSE} = \frac{1}{N} \sum_{i=1}^{N} [(E_{a,i} - \hat{E}_{a,i})^2 + (\lg A_i - \hat{\lg A_i})^2] \tag{10}$$

Model performance was evaluated using coefficient of determination (R^2), root mean squared error (*RMSE*), and mean absolute error (*MAE*):

$$R^2 = 1 - \sum_{i=1}^{n} \frac{(y_i - \hat{y}_i)^2}{\sum_{i=1}^{n} (y_i - \bar{y})^2}, \tag{11}$$

$$RMSE = \sqrt{\frac{1}{n} \sum_{i=1}^{n} (y_i - \hat{y}_i)^2} \tag{12}$$

$$MAE = \frac{1}{n} \sum_{i=1}^{n} |y_i - \hat{y}_i| \tag{13}$$

3. Results and discussion

3.1. Thermal degradation characteristics of NCM cathodes

Fig. 4 presents the thermal decomposition profiles of NCM cathode materials (NCM811, NCM622, NCM523, and NCM111) under 5% H_2/Ar

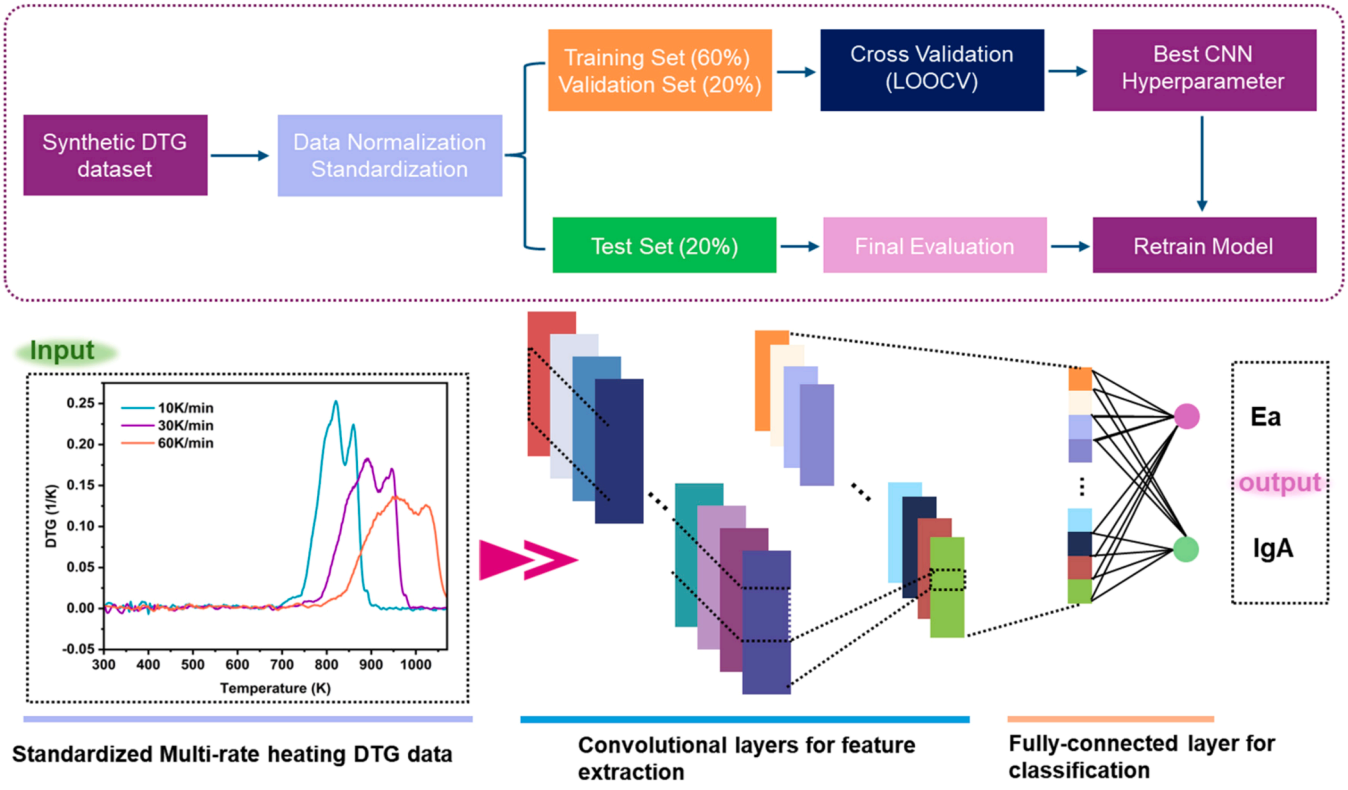

Fig. 3. Architecture of the developed CNN model.

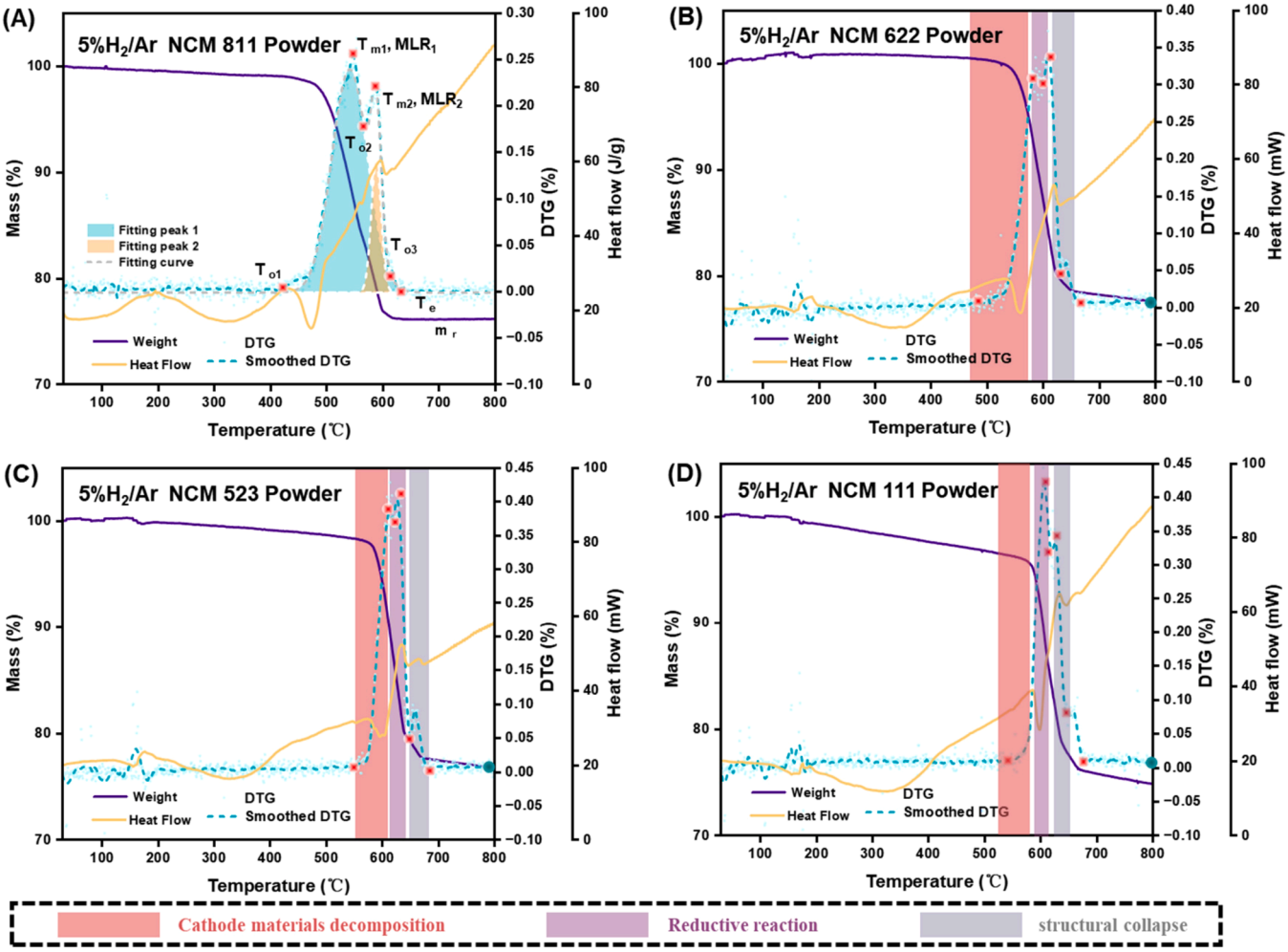

Fig. 4. Non-isothermal decomposition behavior of various cathodes in 5%H_2/Ar (A) NCM 811, (B) NCM 622, (C) NCM 523, (D) NCM 111.

atmosphere, revealing the complex multi-stage decomposition processes through simultaneous thermogravimetric analysis (TGA), differential thermogravimetric analysis (DTG), and differential scanning calorimetry (DSC) measurements. The detailed curve analysis has been thoroughly addressed in our previous work and is therefore not repeated here [9]. The thermal decomposition behavior can be systematically divided into three distinct stages, as indicated by the color-coded regions in Fig. 4. The initial decomposition stage represents the intrinsic thermal breakdown of the layered cathode structure, which is the most critical phase determining the onset of thermal hazards. During this stage, the layered NCM structure undergoes primary decomposition according to the following reaction pathway:

(I)

$$LiNi_xCo_yMn_zO_2(\text{layer}) \rightarrow$$

$$i\,Li_2O + x\,NiO(\text{rock}-\text{salt}) + y\,LiCoO_2(\text{spinel}) + z\,LiMnO_2(\text{spinel}) + O_2(g) \quad (14)$$

$$3LiCoO_2(\text{spinel}) \rightarrow 1.5\,Li_2O + Co_3O_4\ (\text{rock}-\text{salt}) + 0.25\,O_2(g) \quad (15)$$

$$LiCoO_2(\text{spinel}) \rightarrow 0.5\,Li_2O + CoO\ (\text{rock}-\text{salt}) + 0.25\,O_2(g) \quad (16)$$

As hydrogen continues to flow and the temperature rises, the cathode undergoes decomposition into a rock-salt phase, followed by further reduction to metallic species. The second stage involves hydrogen-mediated reduction of decomposition products:

(II)

$$NiO + H_2 \rightarrow Ni + H_2O \quad (17)$$

$$Co_3O_4 + 4\,H_2 \rightarrow 3\,Co + 4\,H_2O \quad (18)$$

$$CoO + H_2 \rightarrow Co + H_2O \quad (19)$$

The weak DTG peaks observed before the cathode mass stabilizes can be attributed to the structural collapse of $LiMnO_2$ as

(III)

$$2LiMnO_2\ (\text{spinel}) \rightarrow Mn_2O_3\ (\text{rock}-\text{salt}) + Li_2O \quad (20)$$

3.2. Composition-driven JMA kinetic stability

Since Stage I largely dictates when thermal instability begins, the kinetic analysis in this work focuses on the primary decomposition step. For this reaction, the conversion degree α corresponds to the extent of layered-structure degradation and the accompanying oxygen release. As shown in Eq. (6), the Johnson-Mehl-Avrami (JMA) kinetic model provides an appropriate framework for describing this solid-state transformation. In the context of NCM decomposition, α represents the fraction of $LiNi_xCo_yMn_zO_2$ that has undergone structural transformation from layered to rock-salt/spinel phases. The Avrami exponent n reflects the nucleation and growth mechanisms during the phase transformation process, while E_a and A characterize the energy barrier and frequency factor for breaking the Ni-O, Co-O, and Mn-O bonds in the layered structure.

The experimental DTG peaks correspond to the maximum reaction rate $(d\alpha/dT)_{max}$ for the transformation of NCM to products, occurring when the thermal energy overcomes the activation barrier for bond breaking and structural rearrangement. The observed peak temperatures directly reflect the material-specific activation energies required to initiate the decomposition pathway described in Eq. (14-16).

This kinetic framework enables quantitative characterization of the NCM thermal decomposition process, where $E_a$and lg$A$ serve as fundamental descriptors of the chemical bond stability and reaction kinetics governing the layered-to-rock-salt phase transformation. These parameters provide the essential input features for machine learning models to predict thermal decomposition behavior across different NCM compositions.

Fig. 5 shows the JMA kinetic model applied to experimental DTG data at different heating rates for all four NCM cathode materials. The JMA model parameters (Ea, lgA, n) were determined through a robust optimization procedure using a differential evolution algorithm, where the kinetic model described by Eq. (6) was numerically integrated to generate theoretical DTG curves according to:

$$\alpha(T) = \int_{T_0}^{T} \frac{A}{\beta}\exp(-\frac{E_a}{RT})\cdot n(1-\alpha)[-\ln(1-\alpha)]^{(n-1)/n}dT' \quad (21)$$

The theoretical DTG curves were calculated from dα/dT and fitted to the experimental data using a composite objective function that simultaneously minimized correlation error, peak-temperature deviation, and mean squared error. Material-dependent parameter bounds were applied to ensure physically meaningful solutions, with E_a constrained between 120–280 kJ/mol depending on composition, lg$A$ between 6.0–17.0, and the Avrami exponent n between 0.3–1.2.

The fitted results show strong agreement with the experimental DTG curves, with correlation coefficients $R^2 > 0.89$ for all samples, demonstrating that the JMA model adequately describes the thermal decomposition behavior of NCM materials. Across all compositions and heating rates, R^2 ranges from 0.899 to 0.966, with NCM622 and NCM111 exhibiting slightly better fits than NCM811 and NCM523. Multi-rate analysis further reveals systematic kinetic trends: higher heating rates lead to increased apparent activation energies, consistent with the kinetic compensation effect. The peak-temperature shifts follow the expected Kissinger relationship, with NCM811 displaying the greatest temperature sensitivity (a 245 °C shift between 10–60 K/min), attributable to its higher Ni content and reduced structural stability.

The extracted kinetic parameters display clear composition dependence: Ea increases in the order NCM811 (143–161 kJ/mol) < NCM622 (195–228 kJ/mol) < NCM523 (202–230 kJ/mol)< NCM111 (231–247 kJ/mol). This trend aligns with the thermal stability hierarchy shown in Fig. 1, confirming that high-Ni cathodes require lower energy to undergo structural decomposition. The logarithmic pre-exponential factors show parallel trends, ranging from 8.45 to 9.18 for NCM811, while 12.16–14.09 for NCM111, indicating that both kinetic parameters correlate strongly with composition-dependent structural stability.

3.3. Adaptive KCE-compositional mapping

Fig. 6 illustrates the kinetic benchmark established for the thermal decomposition of NCM811 via a synchronous multi-rate inversion process. By simultaneously fitting the JMA model to experimental DTG sequences at 10, 30, and 60 K·min^{-1}, this analysis defines the intrinsic parameter space and confirms the physical fidelity of the synthetic datasets utilized for neural network training. To maintain mechanistic consistency across heating scales, an apparent Avrami exponent of n = 3.0 was implemented. This value was identified through parametric optimization as the optimal configuration to minimize global residuals while accurately replicating the asymmetric topology and peak-width evolution characteristic of NCM811 decomposition. The explored parameter space spans the defined ranges for NCM811 (E_a =

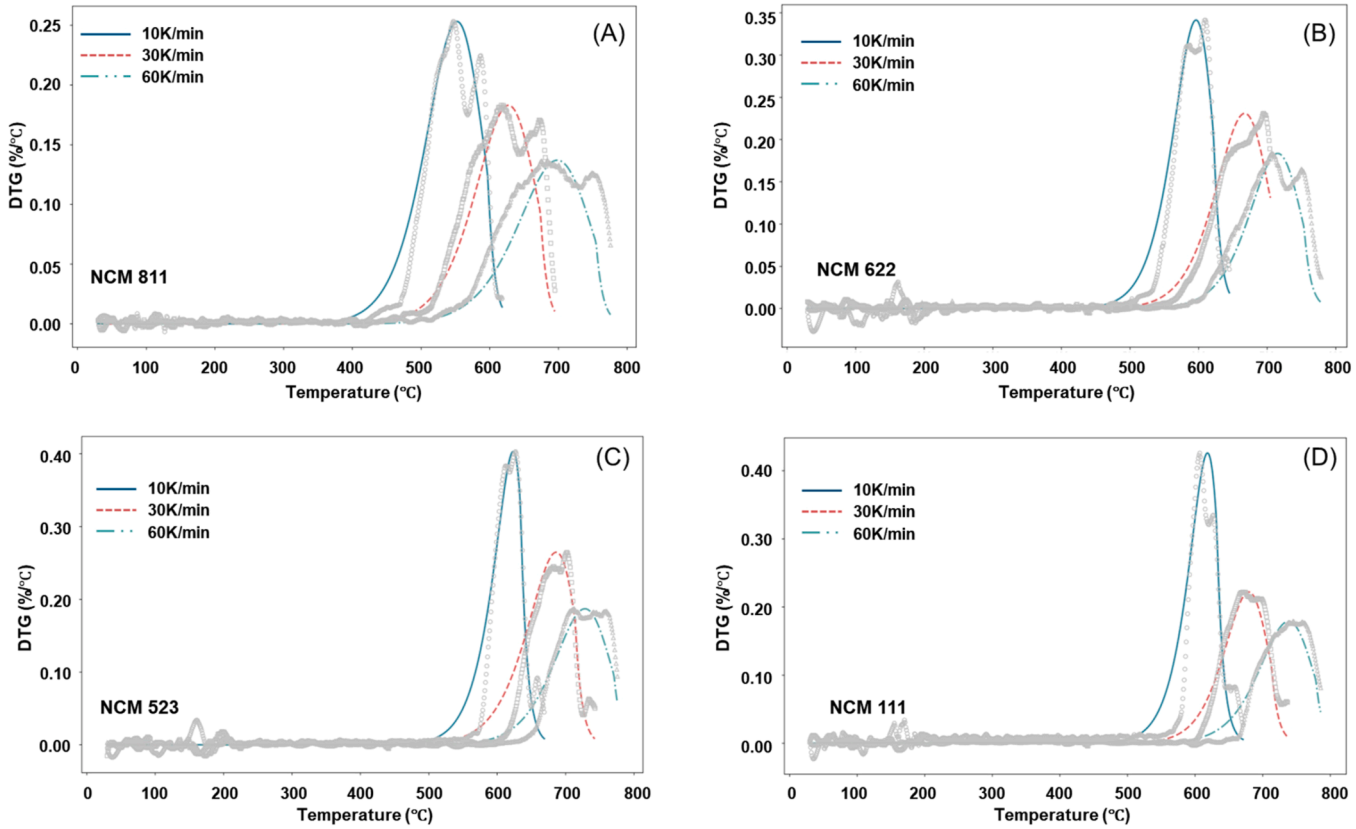

Fig. 5. DTG of cathode materials in 5%H_2/Ar as a function of temperature for three heating rates. (A) NCM811, (B) NCM622, (C) NCM523, (D) NCM111.

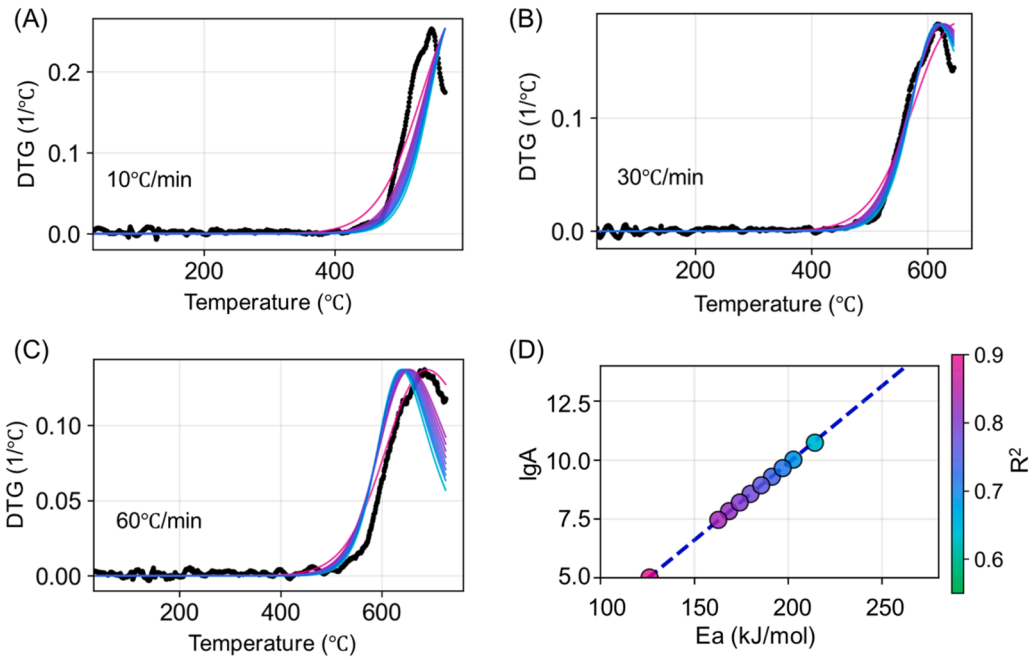

Fig. 6. The kinetic compensation effect (KCE) analysis and model validation for NCM811 thermal decomposition: (A-C) representative DTG fits at 10,30,60℃/min, (D) KCE linear relationship.

100–280 kJ/mol; lg$A$ = 4–14). By fixing the mechanistic parameter n, the mathematical correlation between E_a and lg$A$ was effectively decoupled, enabling a rigorous evaluation of the underlying kinetic compensation effect (KCE).

MEP_L_fig6Fig. 6(A)–(C) demonstrate the high congruency between experimental trajectories (black dots) and the inverted kinetic profiles (colored lines). The model effectively captures the holistic peak evolution, including the systematic temperature-dependent shifts across the 10–60 K·min^{-1} range. The inversion achieved a mean R^2 of 0.894 for the primary solution, with individual R^2 values at 30 K/min frequently exceeding 0.96.

Fig. 6(D) summarizes statistical indicators of the KCE linearity, confirming the robustness of the compensation relationship. Representative fits in Fig. 6(A-C) illustrate the agreement between experimental and calculated DTG curves for several E_a values, with R^2 values ranging from 0.64 to 0.89. The resulting linear relationship, lg$A$ = 0.0655 E_a − 3.25 (R^2 = 0.99), indicates a strong compensation effect in which increases in activation energy are offset by proportional adjustments in the pre-exponential factor. This strictly linear manifold provides the necessary physics-informed constraints for generating the synthetic dataset used in CNN training. The strong KCE behavior ensures that even as E_a and lg$A$ vary, the resulting synthetic DTG curves remain physically

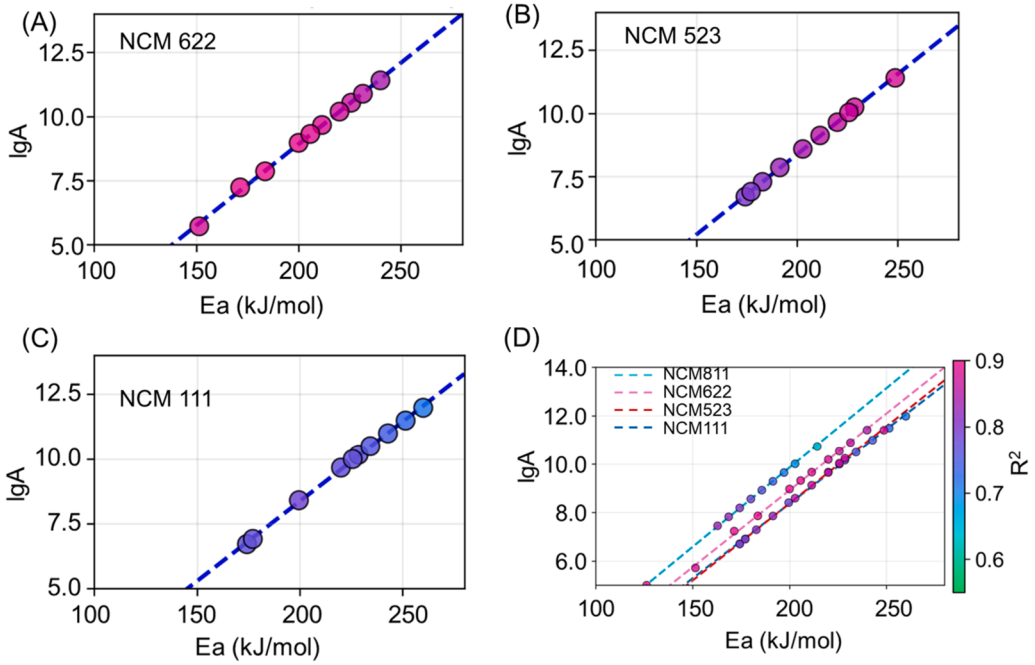

Fig. 7. The adaptive kinetic compensation effect analysis for (A) NCM622, (B) NCM523, and (C) NCM111 materials, (D) KCE relationship for multiple cathode materials.

sound and representative of authentic thermal decomposition trends. This provides a dependable foundation for the subsequent deep learning sections, where these datasets enable the model to internalize the thermodynamic boundaries governing NCM811 degradation under diverse testing conditions.

The KCE relationships of the different NCM cathode materials in Fig. 7 show clear linear trends, with slopes and intercepts that vary systematically with composition. Although the specific linear parameters differ among NCM622, NCM523, and NCM111, the overall behavior indicates that each material follows a well defined compensation pattern. The slopes reflect how sensitively the pre-exponential factor adjusts when the activation energy changes, whereas the intercepts represent the baseline kinetic behavior when the energy barrier is relatively low. These variations capture the intrinsic differences in thermal stability and decomposition pathways among the three materials.

Table 2 establishes a comparative baseline by fixing the lg$A$, enabling a "laterally equivalent" kinetic assessment across diverse material compositions. This approach effectively circumvents the ambiguity inherent in evaluating thermal stability caused by the strong mathematical coupling between $E_a$and lg$A$, a phenomenon known as the kinetic compensation effect (KCE). Using lg$A$ = 9 as the reference, the E_a of the four materials are ordered as follows: NCM811 (186.89 kJ/mol) < NCM622 (201.29 kJ/mol) < NCM523 (209.80 kJ/mol) < NCM111 (210.36 kJ/mol). This numerical trend aligns closely with the experimentally observed hierarchy of thermal stability. A meaningful physical trend emerges from the comparison of KCE parameters across compositions. Materials with higher nickel content generally exhibit steeper KCE slopes (e.g., 0.0655 for NCM811 and 0.0616 for NCM111), suggesting that Ni-rich cathodes possess a more “tightly coupled” kinetic regime. This heightened sensitivity may consistent with the lower structural stability and more flexible decomposition routes inherent to the Ni-rich environment. In contrast, the lower intercepts and rightward shift of the manifolds for Mn-rich materials reflect a higher energy barrier for the initiation of decomposition, aligning with the stabilizing effect of the manganese-rich layered framework.

Despite the wide span of kinetic parameters used for each material, the fits remain consistently accurate, demonstrating that the compensation-based approach can reliably reproduce the thermal decomposition behavior of various NCM systems. These material-specific KCE parameters serve as the governing constraints for our physics-informed synthetic dataset. By internalizing these distinct linear manifolds, the 1D CNN model is trained to distinguish between subtle compositional “fingerprints” within the raw DTG signal topology. This integration ensures that the deep learning framework remains anchored in the thermodynamic realities of the NCM system, providing a dependable foundation for real-time safety assessment and high-throughput material screening.

3.4. Construction of a physics-constrained synthetic DTG dataset

The synthetic dataset for CNN training was constructed via a physics-constrained sampling strategy, ensuring that the 20,000 multi-rate samples (60,000 individual DTG curves) both reflect experimental realities and possess sufficient diversity for deep learning generalization. Fig. 8 summarizes the resulting parameter distributions and representative signal morphologies. To ensure the 1D-CNN internalizes both the governing kinetic laws and the stochastic nature of experimental measurements, we implemented a bifurcated sampling strategy for the E_a, lg$A$ parameter space. Rather than relying on a purely random distribution, the dataset was strategically synthesized to balance physical fidelity with the need for broad feature coverage. The primary population (~75% of total samples) was anchored directly to the material-specific KCE manifolds established in test data analysis.

For each NCM formulation, E_a values were sampled uniformly within their respective stability windows, while the corresponding lg$A$ values were derived through the calibrated KCE equations. Crucially, to emulate the inherent scatter found in real-world TGA/DSC data, a zero-mean Gaussian jitter (σ = 0.5 in lg$A$) was superimposed onto these values. This transforms the idealized linear relationships into a “kinetic band” that more accurately reflects the experimental uncertainty and the effective parameter spread observed across different NCM ratios. This physics-centric distribution was then augmented by a stochastic expansion (~25% of samples), where (E_a, lgA) pairs were drawn independently from a uniform plane encompassing E_a in [120, 260] kJ//mol and lgA in [4,14].

This design choice is critical for preventing the model from overfitting strictly to the linear KCE clusters. By exposing the network to a broader spectrum of “off-line” kinetic configurations, the CNN develops the necessary robustness to generalize across anomalous decomposition behaviors and outliers that may arise during practical thermal runaway assessments. The resulting joint distribution, visualized in the (E_a, lg$A$) scatter plot (Fig. 8C), provides a comprehensive and diverse training base that remains firmly grounded in the thermodynamic realities of the NCM system. Representative synthetic DTG triplets are showcased in Fig. 8(D), illustrating the broad morphological diversity generated by the bifurcated sampling scheme. The plot compares two distinct kinetic scenarios: a relatively low-barrier case (Ea = 135.1 kJ/mol, lg$A$ = 11.4) and a high-stability instance (Ea = 251.2 kJ/mol, lg$A$ = 11.77).

3.5. Performance of 1D CNN and implications for thermal-safety assessment

The multi-heating rate CNN is engineered as a multi-modal regression framework to extract kinetic descriptors directly from raw TGA trajectories. The input architecture adopts a synchronized multi-channel strategy, where three normalized DTG sequences are resampled to 200 equidistant points and stacked as a 3-channel 1D tensor. This configuration allows the network to simultaneously resolve the temperature-dependent peak shifts and the asymmetric signal topologies characteristic of the NCM decomposition process. A shared 1D-CNN backbone is utilized for high-level feature extraction across the DTG channels. This backbone comprises four convolutional layers with channels expanding from 32 to 256, while kernel sizes are systematically tapered from 15 to 3 to capture both broad thermal envelopes and fine-grained reaction features. To ensure numerical stability and prevent overfitting, each

Table 2
Summary of KCE relationship for multiple cathode materials, where the characteristic temperatures are measured under the TGA heating rate of 30 K/min.

Cathode	NCM811	NCM622	NCM523	NCM111
T_{onset} (℃)	484	564	607	603
T_{peak} (℃)	617	644	683	671
KCE formula	$lgA = 0.0655E_a - 3.25$	$lgA = 0.0635E_a - 3.78$	$lgA = 0.0636E_a - 4.35$	$lgA = 0.0616E_a - 3.95$
Fixed lg$A$ (s^{-1})	E_a (kJ/mol)	E_a (kJ/mol)	E_a (kJ/mol)	E_a (kJ/mol)
5	125.85	138.25	146.93	145.38
7	156.37	169.77	178.36	177.87
9	186.89	201.29	209.80	210.36
11	217.41	232.81	241.24	242.85
13	247.92	264.33	272.67	275.34

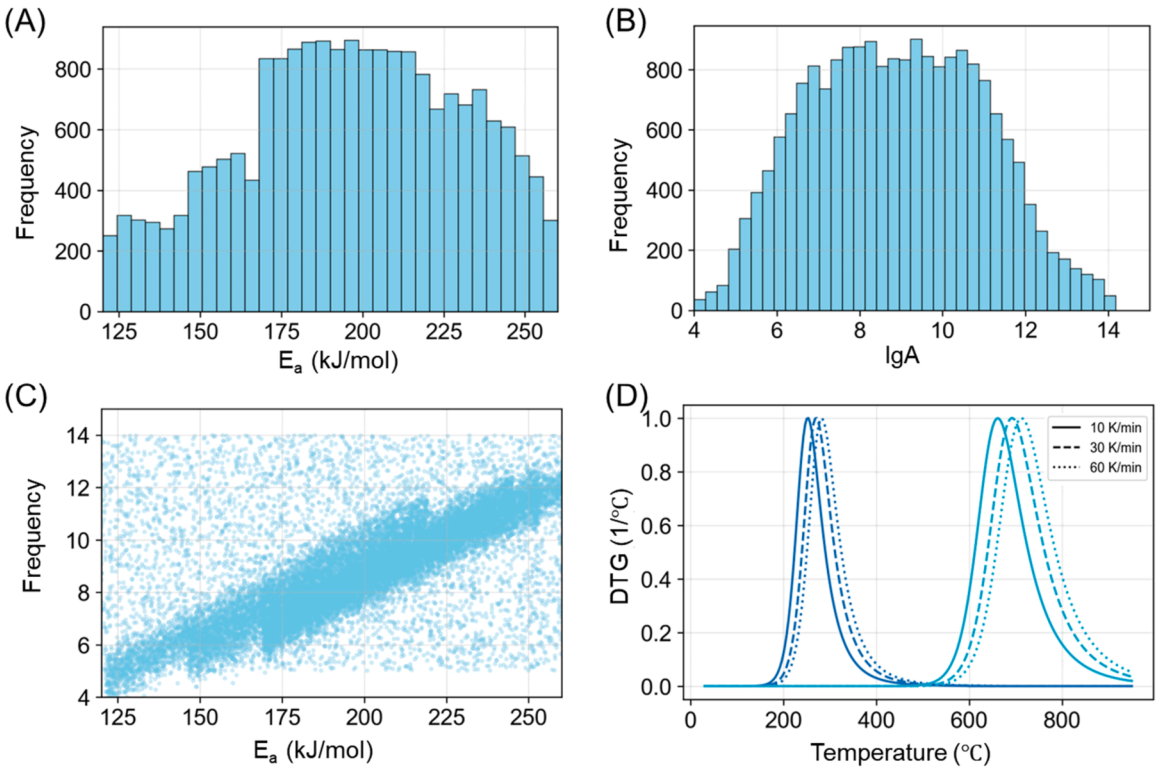

Fig. 8. The comprehensive parameter distribution analysis for the synthetic DTG dataset generation: (A) E_a distribution by cathode materials, (B) lg$A$ distribution by cathode materials, (C) kinetic compensation effect scatter plot, (D) representative synthetic DTG triplets.

convolutional stage integrates batch normalization and dropout (0.2–0.3). The resulting embeddings are flattened and concatenated with a 3-dimensional heating rate vector, forming a unified feature representation that encodes both the signal morphology and the corresponding experimental conditions.

The final regression to E_a and lg$A$ is performed by a deep fully connected head with a decreasing neuron density (256–128–64–32–2). In total, the model contains approximately 2.3×10^5 trainable parameters and was optimized using the MSE loss function. Training was executed on a curated dataset of 20,000 multi-rate samples using a 70/15/15 train–validation–test split. Optimization was driven by the Adam optimizer ($lr = 3 \times 10^{-4}$) with a cosine-annealing learning-rate schedule (T_{max}= 140) to facilitate precise convergence within the complex kinetic parameter space. As illustrated in Fig. 9, the training history demonstrates smooth and stable convergence. Both training and validation losses decrease monotonically to a low plateau, with the training R^2 reaching approximately 0.94 and the validation R^2 stabilizing at 0.92. The close overlap between the two curves confirms that the regularization strategy and adaptive learning-rate schedule help prevent overfitting.

Fig. 10 illustrates the alignment between the CNN-predicted coordinates and the reference KCE lines across the cathode materials series. This validation was established through an integrated pipeline where experimental DTG data were first inverted via the JMA model (n = 3) to define the ground-truth KCE benchmarks, represented by the blue dashed lines across the NCM811–111 series. Subsequently, the trained network performed forward inference on synthetic DTG triplets sampled along these trajectories, producing the orange clusters that characterize the CNN's learned parameter space.

By applying a secondary linear regression to these predicted clusters, the resulting "Pred" equations reveal a remarkably high degree of overlap with the reference benchmarks across the entire energetic range. In the specific case of NCM811 (Fig. 10A), the reconstructed relationship of lg$A$ = 0.0652 E_a - 3.315 is nearly indistinguishable from the reference

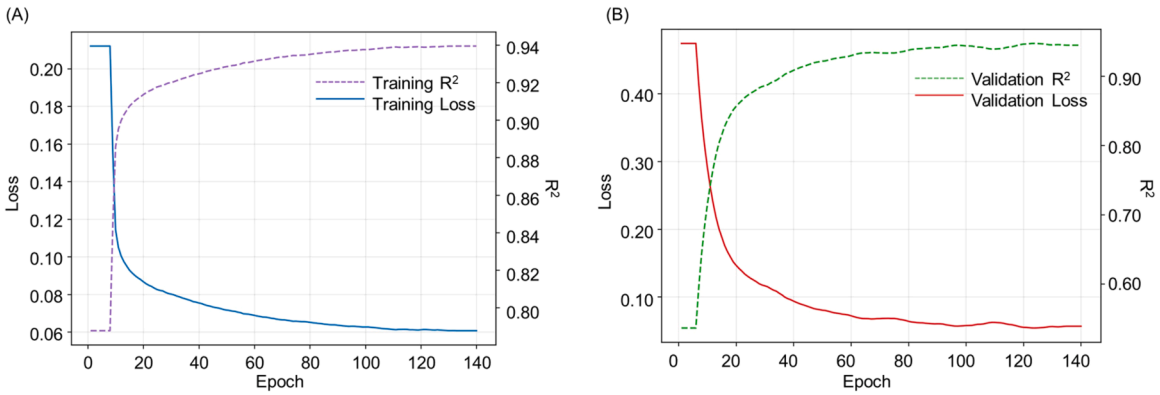

Fig. 9. Training progress monitoring: (A) Training set, (B) Validation set.

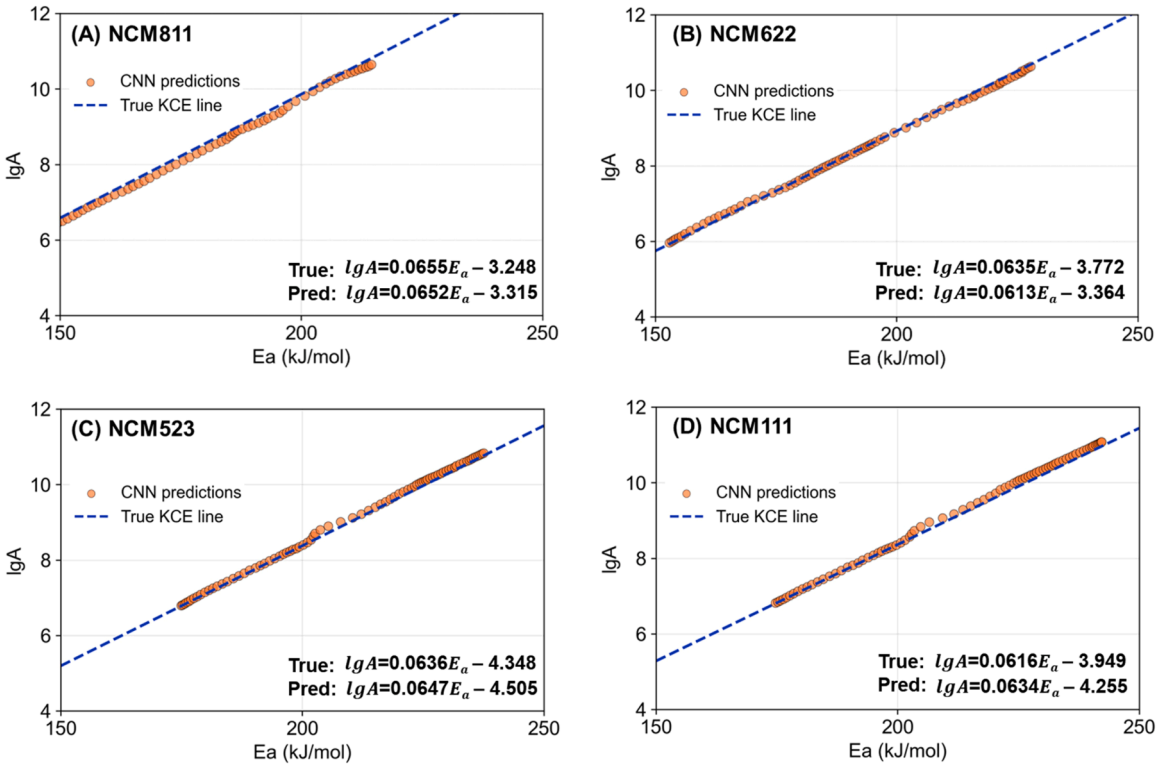

Fig. 10. Comparison of CNN-predicted (E_a, lg$A$) with reference KCE lines for (A) NCM811, (B) NCM622, (C) NCM523, and (D) NCM111.

line of lg$A$ = 0.0656 E_a - 3.248, representing a slope deviation of less than 0.5%. Such precision confirms that the 1D-CNN has successfully internalized the Arrhenius-based thermodynamic constraints, accurately reproducing the coupling between the energetic barrier and the frequency factor with negligible numerical drift.

Beyond numerical accuracy, the model consistently preserves the characteristic slope hierarchy inherent in the NCM system, effectively distinguishing the steeper gradients of Ni-rich formulations from the flatter profiles of Mn-rich ones. This alignment proves that the multi-channel feature extraction process is sensitive enough to capture the global "kinetic fingerprints" of the NCM system without requiring explicit material labels. By bypassing the inherent subjectivity of manual curve-fitting, this framework establishes a dependable, high-throughput route to obtain physically consistent descriptors, bridging raw laboratory measurements with standardized safety assessments in large-scale energy storage systems.

Additionally, moving from labor-intensive manual optimization to a single forward pass reduces calculation time from hours to milliseconds. This speed enables the high-throughput safety screening of vast material libraries. The accurate reconstruction of KCE lines for each composition confirms that the model has successfully captured the Arrhenius laws governing cathode decomposition. This capability establishes a strong basis for real-time safety diagnostics in large-scale energy storage systems. In these applications, identifying kinetic parameters quickly is vital for predicting and mitigating thermal runaway across various cathode chemistries.

4. Conclusions

This study presents a data-driven framework that bridges thermal safety assessment and quantitative kinetic analysis through physically informed deep learning. By training on a large-scale JMA/KCE-constrained dataset of 20,000 multi-rate samples, the developed Multi-Heating Rate CNN directly extracts the E_a and lg$A$ from synchronized DTG sequences of pristine NCM cathodes, eliminating the need for manual curve fitting and feature engineering. Across four NCM cathode compositions (NCM811, NCM622, NCM523, NCM111) under 5% H_2/Ar reductive atmosphere, the CNN demonstrates consistent accuracy (R^2=0.94 for training set, R^2= 0.92 for validation set).

The framework's ability to faithfully reconstruct material-specific kinetic manifolds with slope deviations under 0.5% confirms that it has successfully internalized the Arrhenius-based thermodynamic constraints governing cathode degradation. By autonomously resolving the thermal lag across multiple heating scales, the CNN functions as a high-throughput "kinetics intelligence" engine. It reduces the diagnostic latency from hours to milliseconds, providing a scalable and reproducible tool for early-stage thermal runaway risk assessment in battery design workflows.

The current focus on "effective kinetics" via a one-step JMA description of pristine materials is a strategic simplification aimed at establishing a high-fidelity physical baseline. While delithiated cathodes exhibit more complex, multi-stage reaction pathways critical to practical thermal runaway, this pristine-based foundation provides the necessary signal-to-noise ratio to validate the 1D-CNN's feature extraction capabilities. By targeting the primary mass loss event as a key descriptor for safety screening at early stages, this work provides a dependable kinetics intelligence framework. As standardized experimental databases expand, the current architecture will serve as a pretrained foundation for future models with multiple outputs designed to resolve coupled reaction networks.

Overall, this study demonstrates that physically informed, data-driven analysis of DTG curves can deliver fast, reliable, and scalable kinetic parameter predictions, paving the way for broader adoption of "kinetics intelligence" in battery research and safety assessment. The framework offers a scalable and reproducible tool that bridges the gap between laboratory-scale kinetic analysis and industrial-scale material screening, supporting the development of safer and more efficient battery systems.

CRediT authorship contribution statement

Yichao Zhang: Validation, Conceptualization. **Yuxin Zhou:** Validation, Formal analysis, Data curation, Conceptualization. **Shaorun Lin:** Writing – original draft, Formal analysis, Data curation. **Xinyan Huang:** Writing – review & editing, Funding acquisition, Formal analysis, Conceptualization. **Peiyi Sun:** Methodology, Data curation. **Yifei Ding:** Methodology, Formal analysis.

Consent for publication

Yes.

Financial support and sponsorship

This work is supported by the National Key Research and Development Program of China (No.2024YFE0209200). The authors also thank the support from PolyU Research Institute for Smart Energy.

Declaration of Competing Interest

The authors declare that they have no known competing financial interests or personal relationships that could have appeared to influence the work reported in this paper.

Data availability

Data will be made available on request.

References

[1] F. Mohammadi, M. Saif, A comprehensive overview of electric vehicle batteries market, E-Prime - Adv. Electr. Eng. Electron. Energy 3 (2023) 100127, https://doi.org/10.1016/j.prime.2023.100127.
[2] X. Yang, H. Zhang, Q. Liu, G. Jiang, The Li-ion battery industry and its challenges, Nat. Rev. Chem. 9 (2025) 497–498, https://doi.org/10.1038/s41570-025-00742-2.
[3] H. Du, Y. Wang, Y. Kang, Y. Zhao, Y. Tian, X. Wang, et al., Side reactions / changes in lithium-ion batteries: mechanisms and strategies for creating safer and better batteries, Adv. Mater. (2024) 2401482, https://doi.org/10.1002/adma.202401482.
[4] X. Feng, D. Ren, X. He, M. Ouyang, Mitigating thermal runaway of lithium-ion batteries, Joule 4 (2020) 743–770, https://doi.org/10.1016/j.joule.2020.02.010.
[5] X. Feng, M. Ouyang, X. Liu, L. Lu, Y. Xia, X. He, Thermal runaway mechanism of lithium ion battery for electric vehicles: a review, Energy Storage Mater. 10 (2025) 246–267, https://doi.org/10.1016/j.ensm.2017.05.013.
[6] S. Sharifi-asl, J. Lu, K. Amine, R. Shahbazian-yassar, Oxygen release degradation in li-ion battery cathode materials: mechanisms and mitigating approaches, Adv. Energy Mater. (2019) 1–19, https://doi.org/10.1002/aenm.201900551.
[7] Y. Wang, D. Ren, X. Feng, L. Wang, M. Ouyang, Thermal kinetics comparison of delithiated Li[NixCoyMn1-x-y]O2 cathodes, J. Power Sources 514 (2021) 230582, https://doi.org/10.1016/j.jpowsour.2021.230582.
[8] Y. Wang, X. Feng, Y. Nitta, M. Ouyang, Y. Wang, X. Feng, et al., Article Reductive gas manipulation at early self- heating stage enables controllable battery thermal failure Reductive gas manipulation at early self-heating stage enables controllable battery thermal failure, Joule 6 (2022) 2810–2820, https://doi.org/10.1016/j.joule.2022.10.010.
[9] Y. Zhou, Y. Ding, Y. Chen, Y. Shen, Z. Wang, X. Li, et al., Thermal degradation of lithium-ion battery cathodes: a machine learning prediction of stability and safety, Energy Mater. (2025), https://doi.org/10.20517/energymater.2024.200.
[10] D.D. Macneil, J.R. Dahn, Test of reaction kinetics using both differential scanning and accelerating rate calorimetries as applied to the reaction of $LixCoO_2$ in non-aqueous electrolyte, Am. Chem. Soc. (2001) 4430–4439, https://doi.org/10.1021/jp001187j.
[11] Y. Furushima, C. Yanagisawa, T. Nakagawa, Y. Aoki, N. Muraki, Thermal stability and kinetics of delithiated $LiCoO_2$, J. Power Sources J. 196 (2011) 2260–2263, https://doi.org/10.1016/j.jpowsour.2010.09.076.
[12] D.D. MacNeil, L. Christensen, J. Landucci, J.M. Paulsen, J.R. Dahn, An Autocatalytic mechanism for the reaction of Lix CoO_2 in electrolyte at elevated temperature, J. Electrochem. Soc. 147 (2000) 970.
[13] D.D. MacNeil, J.R. Dahn, The reactions of $Li_{0.5}CoO_2$ with nonaqueous solvents at elevated temperatures, J. Electrochem. Soc. 149 (2002) A912, https://doi.org/10.1149/1.1483865.
[14] J. Yamaki, J. Electrochem, A. Soc, J. Yamaki, Y. Shinjo, T. Doi, et al., The rate equation for oxygen evolution by decomposition of Li_xCoO_2 at elevated temperatures the rate equation for oxygen evolution by decomposition of Li_xCoO_2 at elevated temperatures, J. Electrochem. Soc. (2014), https://doi.org/10.1149/2.0621410jes.
[15] R.L. Blaine, H.E. Kissinger, Thermochimica acta homer kissinger and the kissinger equation, Thermochim. Acta 540 (2012) 1–6, https://doi.org/10.1016/j.tca.2012.04.008.
[16] S. Vyazovkin, A.K. Burnham, J.M. Criado, L.A. Pérez-maqueda, C. Popescu, N. Sbirrazzuoli, Thermochimica Acta ICTAC kinetics committee recommendations for performing kinetic computations on thermal analysis data, Thermochim. Acta 520 (2011) 1–19, https://doi.org/10.1016/j.tca.2011.03.034.
[17] S. Vyazovkin, Kissinger method in kinetics of materials: things to beware and be aware of, Molecules (2020), https://doi.org/10.3390/molecules25122813.
[18] B.C. Koenig, P. Zhao, S. Deng, Accommodating physical reaction schemes in DSC cathode thermal stability analysis using chemical reaction neural networks, J. Power Sources 581 (2023) 233443, https://doi.org/10.1016/j.jpowsour.2023.233443.
[19] B.C. Koenig, P. Zhao, S. Deng, Comprehensive thermal-kinetic uncertainty quantification of lithium-ion battery thermal runaway via bayesian chemical reaction neural networks, Chem. Eng. J. 507 (2025) 160402, https://doi.org/10.1016/j.cej.2025.160402.
[20] N. Karathanasopoulos, P. Hadjidoukas, Advanced Engineering Informatics Deep learning based automated fracture identification in material characterization experiments, Adv. Eng. Inform. 60 (2024) 102402, https://doi.org/10.1016/j.aei.2024.102402.
[21] C. Rao, Y. Liu, Three-dimensional convolutional neural network (3D-CNN) for heterogeneous material homogenization, Comput. Mater. Sci. 184 (2020) 109850, https://doi.org/10.1016/j.commatsci.2020.109850.
[22] W. Nash, T. Drummond, N. Birbilis, A review of deep learning in the study of materials degradation, Npj Mater. Degrad. (2018) 1–12, https://doi.org/10.1038/s41529-018-0058-x.
[23] X. Wang, Z. Zhou, S. He, J. Liu, W. Cui, Performance degradation modeling and its prediction algorithm of an igbt gate oxide layer based on a CNN-LSTM network, Micro. (2023), https://doi.org/10.3390/mi14050959.
[24] J. Masci, U. Meier, D. Cireşan, et al., Stacked convolutional auto-encoders for hierarchical feature extraction[C]. International conference on artificial neural networks, Springer Berlin Heidelberg, Berlin, Heidelberg, 2011, pp. 52–59, https://doi.org/10.1007/978-3-642-21735-7_7 (//).
[25] G. Cheng, Z. Li, J. Han, X. Yao, L. Guo, Exploring hierarchical convolutional features for hyperspectral image classification, IEEE Trans. Geosci. Remote Sens. 56 (2018) 6712–6722, https://doi.org/10.1109/TGRS.2018.2841823.
[26] K. Rana, G. Singh, P. Goyal, MSRD-CNN: multi-scale residual deep CNN for general-purpose image manipulation detection, IEEE Access 10 (2022) 41267–41275, https://doi.org/10.1109/ACCESS.2022.3167714.
[27] S.A. El, S. Tarek, M.K. Mohamed, Thermal degradation behaviour and chemical kinetic characteristics of biomass pyrolysis using TG / DTG / DTA techniques, Biomass. Convers. Biorefin 14 (2024) 17779–17803, https://doi.org/10.1007/s13399-023-03926-2.
[28] Y. Chen, Z. Wang, S. Lin, Y. Qin, X. Huang, A review on biomass thermal-oxidative decomposition data and machine learning prediction of thermal analysis, Clean. Mater. (2023) 100206, https://doi.org/10.1016/j.clema.2023.100206.
[29] Y. Wang, D. Ren, X. Feng, L. Wang, M. Ouyang, Thermal runaway modeling of large format high-nickel / silicon-graphite lithium-ion batteries based on reaction sequence and kinetics, Appl. Energy 306 (2022) 117943, https://doi.org/10.1016/j.apenergy.2021.117943.
[30] D. Velumani, A. Bansal, Thermal behavior of lithium- and sodium-Ion batteries: a review on heat generation, battery degradation, thermal runway – perspective and future directions, Energy Fuels 36 (2022) 14000–14029, https://doi.org/10.1021/acs.energyfuels.2c02889.
[31] S. Harbola, V. Coors, One dimensional convolutional neural network architectures for wind prediction, Energy Convers. Manag. 195 (2019) 70–75, https://doi.org/10.1016/j.enconman.2019.05.007.
[32] E. Ul, H. Qazi, A. Almorjan, T. Zia, Applied sciences A One-dimensional convolutional neural network (1D-CNN) based deep learning system for network intrusion detection, Appl. Sci. (2022) 4–17, https://doi.org/10.3390/app12167986.
[33] Y. Xiong, N. Liu, Z. Xu, Y. Zhang, A parameter partial-sharing cnn architecture for cross-domain clothing retrieval, 2016 Vis. Commun. Image Process. (VCIP) (2016) 1–4, https://doi.org/10.1109/VCIP.2016.7805463.
[34] X. Zhang, Applications of kinetic methods in thermal analysis: a review, Eng. Sci. 14 (2021) 1–13, https://doi.org/10.30919/es8d1132.
[35] K. Broeckhoven, Methods to determine the kinetic performance limit of contemporary chromatographic techniques, J. Sep Sci. 44 (2021) 323–339, https://doi.org/10.1002/jssc.202000779.
[36] Y. Liao, L. Han, H. Wang, Prediction models for railway track geometry degradation using machine learning methods: a review, Sensors (2022) 1–26, https://doi.org/10.3390/s22197275.
[37] H.E. Kissinger, Reaction kinetics in differential thermal analysis, Anal. Chem. 29 (11) (1957) 1702–1706.
[38] J.P. Elder, The general applicability of the kissinger equation in thermal analysis, J. Therm. Anal. 30 (2000) 657–669, https://doi.org/10.1007/BF01913612.

[39] F. Liu, G.C. Yang, J.N. Liu, Comparison between an analytical model and JMA kinetics for isothermally and isochronally conducted transformations, Thermochim. Acta 438 (2005) 83–89, https://doi.org/10.1016/j.tca.2005.08.019.
[40] R. Svoboda, Journal of the european ceramic society crystallization of glasses – when to use the johnson-mehl-avrami kinetics ? J. Eur. Ceram. Soc. 41 (2021) 7862–7867, https://doi.org/10.1016/j.jeurceramsoc.2021.08.026.
[41] H. Kim, H. Jo, C. Ryu, Derivation of kinetic parameters and lignocellulosic composition from thermogram of biomass pyrolysis using convolutional neural network, Int. J. Energy Res (2024), https://doi.org/10.1155/er/6184508.